



1 **How are the gravity waves triggered by typhoon propagate from the**
2 **troposphere to upper atmosphere?**

3 Qinzeng Li¹, Jiyao Xu^{1,2}, Hanli Liu³, Xiao Liu⁴, Wei Yuan¹

4 ¹State Key Laboratory of Space Weather, National Space Science Center, Chinese Academy of
5 Sciences, Beijing, 100190, China,

6 ²School of Astronomy and Space Science, University of Chinese Academy of Science, Beijing,
7 100049, China,

8 ³High Altitude Observatory, National Center for Atmospheric Research, Boulder, CO
9 80307-3000, USA,

10 ⁴School of Mathematics and Information Science, Henan Normal University, Xinxiang, 453007,
11 China,

12

13 Correspondence to: xujy@nssc.ac.cn



14 **Abstract**

15 Gravity waves (GWs) strongly affect atmospheric dynamics, and photochemistry, as
16 well as the coupling between the troposphere, stratosphere, mesosphere, and thermosphere.
17 Also, GWs generated by strong disturbances in the troposphere (such as thunderstorms,
18 typhoons, etc.) can affect the atmosphere of the Earth ranging from the troposphere to the
19 thermosphere. However, the fundamental process of GW propagation from the troposphere
20 to the thermosphere is poorly understood because it is challenging to constrain this process
21 by observations. Moreover, GWs tend to dissipate rapidly in the thermosphere because the
22 molecular diffusion increases exponentially. In this study, a double-layer airglow network
23 is used to capture the concentric gravity waves (CGWs) over China, which were excited by
24 the Super Typhoon Chaba (2016). We used the ERA-5 reanalysis data and Multi-functional
25 Transport Satellite-1R observations and quantitatively described the physical mechanism of
26 typhoon-generated CGWs propagating throughout the stratosphere, mesosphere, and
27 thermosphere. We found that the CGWs in the mesopause region were generated directly by
28 the typhoon in the troposphere. However, the backward ray tracing analysis revealed that
29 CGWs in the thermosphere originated from the secondary waves generated by the
30 dissipation of the CGW in the mesopause region, thereby resembling the relay in the
31 context.

32

33

34

35



36 **1. Introduction**

37 Gravity waves (GWs) can transfer momentum and energy from the lower to upper
38 atmospheres, thereby affecting the global circulation and thermal structures, as well as the
39 distribution of chemical composition in the middle and upper atmospheres (Holton, 1983;
40 Fritts and Alexander, 2003). The dynamic, photochemical, and electrodynamic processes
41 have indicated that GWs are fundamental for the coupling process between the troposphere,
42 stratosphere, mesosphere, and thermosphere (Liu and Vadas, 2013; Smith et al., 2013; Vadas
43 and Liu, 2013; Xu et al., 2015).

44 Concentric GWs (CGWs) are unique type of GWs that are considered to be generated
45 by convective activities in the troposphere. CGWs in the stratosphere and mesosphere
46 generated by thunderstorms (Taylor and Hapgood, 1988; Sentman et al., 2003; Suzuki et al.,
47 2007; Yue et al., 2009; Xu et al., 2015; Smith et al., 2020) have been widely reported since
48 their sources are ubiquitous. In previous studies, CGWs induced by typhoons were detected
49 using ground-based optical remote sensing (Suzuki et al., 2013) while those induced by
50 hurricanes and tropical cyclones were detected using the Suomi National Polar-orbiting
51 Partnership satellite (Yue et al., 2014; Xu et al., 2019) in the mesopause region.

52 Notably, GWs tend to dissipate rapidly in the upper atmosphere due to molecular
53 viscosity and thermal diffusion (Vadas, 2007). Thermosphere GWs that are not dissipated
54 can originate directly from the troposphere or from secondary GWs, which are generated as
55 a result of breaking of primary GWs in the mesosphere or thermosphere region (Vadas and
56 Crowley, 2010). Moreover, wave-wave, wave-mean flow, self-acceleration, and nonlinear
57 breaking also signify potential secondary wave generation mechanisms (Lund and Fritts,



58 2012; Fritts et al., 2015; Dong et al., 2020; Fritts et al., 2020; Franke and Robinson, 1999;
59 Zhou et al. 2002; Heale et al. 2020). At the same time, tunneling has been deemed as a
60 mechanism that can couple waves from tropospheric sources to the thermosphere (e.g.
61 Walterscheid and Hecht, 2003, Gavrilov and Kshevetskii, 2018, Heale et al., 2021).
62 However, the lack of observations of the entire atmosphere limits our understanding of the
63 fundamental process of how the GWs propagate from the lower atmosphere to the upper
64 atmosphere step by step on the aspect of observations.

65 This study examined the CGWs excited by Super Typhoon Chaba (2016) as a study
66 case. To this end, we utilized Multi-functional Transport Satellite-1R (MTSAT-1R)
67 observations, multi-layer European Centre for Medium-range Weather Forecasts (ECMWF)
68 ERA-5 reanalysis data (Hoffmann et al., 2019; Hersbach et al., 2020), and high spatio-
69 temporal resolution double-layer airglow network (DLAN) (Xu et al., 2021) observations.
70 The CGW observations from the troposphere to the stratosphere and then to the mesosphere
71 were taken from MTSAT-1R, ERA-5, and DLAN. However, given the observational
72 limitations, the DLAN was utilized to identify the mesosphere and thermosphere via the ray
73 tracing theory. The objectives of this study were to (a) scrutinize multi-layer CGW features
74 produced by Super Typhoon Chaba (2016) from near the ground to a height of 250 km, (b) to
75 examine the entire propagation process of the CGWs excited by typhoon from the lower
76 atmosphere to the upper atmosphere, and (c) to provide new insights into the coupling
77 between different atmospheric layers.

78 **2. Data and Methods**

79 **2.1 Double layer all-sky airglow imager network data**

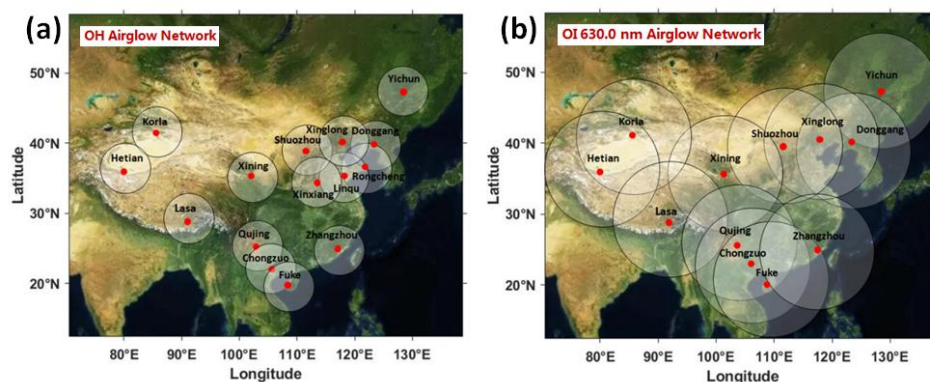


80 The DLAN, including an OH layer (~87 km) and an OI 630.0 nm layer (~250 km)
81 was established over the mainland China. The research aim of DLAN is to explore the
82 physical mechanism of vertical and horizontal propagation, as well as the evolution of
83 atmospheric waves, triggered by severe disasters, such as typhoons, earthquakes, and
84 tsunamis, in various middle and upper atmospheric layers. The OH airglow network
85 comprises 15 stations, including the first no-gap OH airglow all-sky imager network located
86 in northern China (Xu et al., 2015). The OI 630.0 nm airglow network contains 12 stations.
87 Each imager consists of a 1024×1024 pixel back-illuminated CCD detector and a Nikon16
88 mm/2.8D fish-eye lens with a 180 ° field of view (FOV). The OI 630.0 nm imager is operated
89 at the 3.0 nm bandwidth filter with the centre wavelength of 630.0 nm. Observations using
90 airglow optical remote sensing require only a few airglow imagers to cover a wide area,
91 although it is limited by meteorological conditions. Moreover, airglow observations can be
92 used to monitor multi-layer GW activities. Figure 1a and 1b illustrate the OH and OI 630.0
93 nm network station distribution maps, respectively, in China. The OI 630.0 nm network
94 covers nearly the entire mainland China. Furthermore, the DLAN provides an excellent
95 solution for studying the coupling process among different atmospheric layers, especially the
96 mesosphere and thermosphere.

97 Several standard procedures were applied to raw airglow images, including star
98 contamination subtraction, flat fielding to remove van Rhijin, and atmospheric extinction (Li
99 et al., 2011). The GW structure was retrieved by taking the deviation of each processed
100 image from a half-hour running average window image. Finally, the images were projected
101 onto the Earth's surface using the standard star map software and the altitude of the airglow



102 layer (Garcia et al., 1997). The altitudes of the OH and OI 630.0 nm emission layers were set
103 as approximately 87 km and 250 km, respectively.



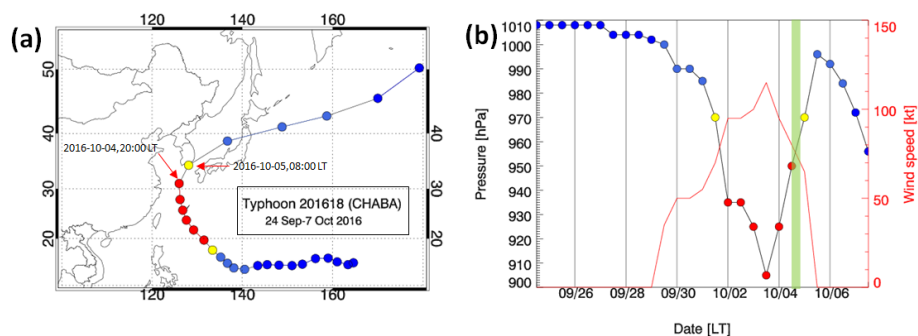
104
105 **Figure 1.** (a) OH airglow all-sky imager network (15 stations). (b) Red line (630 nm) airglow all-sky
106 imager network (12 stations). The circles on the maps give the effective observation ranges of OH and
107 Red line airglow imagers with diameters of about 800 km and 1800 km, respectively.

108 2.2 Development of Super Typhoon Chaba

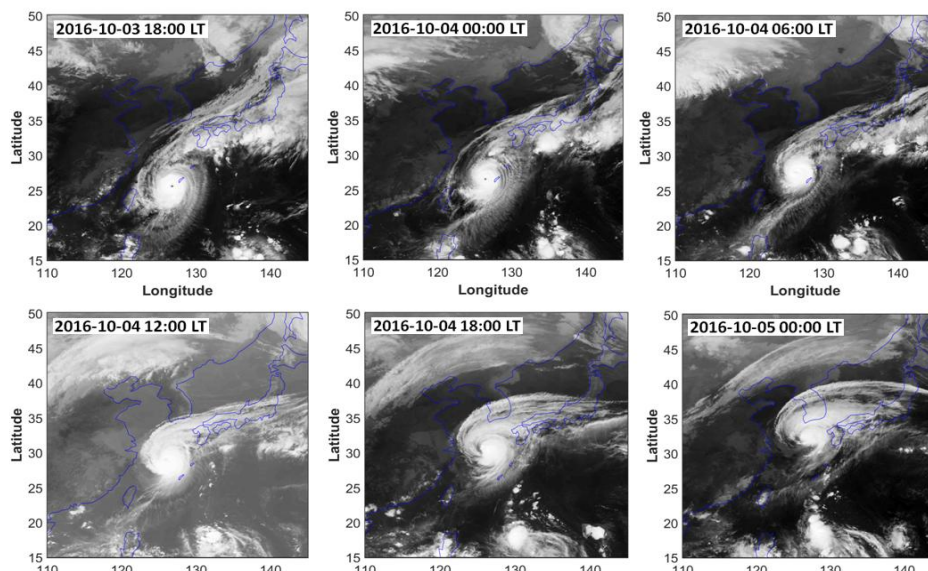
109 Super Typhoon Chaba (2016) developed in the north-western Pacific on 24 September
110 2016 and its track is shown in Fig. 2a. Initially, it moved westward and then turned
111 north-westward on 30 September. The central pressure in the eye of the typhoon and the
112 maximum wind speed are shown in Fig. 2b. On 3 October 2016 at 12:00 UT, the typhoon was
113 in the mature stage with a minimum central pressure of 905 hPa and maximum sustained
114 winds of approximately 59 m/s. The typhoon moved northward on 3 October 2016 at 18:00
115 UT until 4 October 2016 at 18:00 UT. The typhoon continued moving towards the northeast
116 and disappeared on 7 October 2016 at 18:00 UT. Consecutive satellite images of the typhoon
117 from MTSAT-1R from 18:00 LT on 3 October 2016 to 00:00 LT on 5 October 2016 are shown
118 in Fig. 3. MTSAT-1R, which belongs to the Japan Meteorological Agency, comprises a series
119 of Geo-stationary Meteorological Satellites. MTSAT-1R is located at around 140°E and



120 covers East-Asia and western Pacific region. The MTSAT-IR consists of four infrared
121 channels (IR1, IR2, IR3, and IR4) and one visible channel (VIS). The MTSAT- IR1 was used
122 in this study. The track of the typhoon was beyond the effective FOV of the OH network and
123 at the edge of the effective FOV of the OI 630.0 nm network, which provides an excellent
124 example for observing the CGWs stimulated by the typhoon and studying the coupling among
125 the atmospheric layers.



126
127 **Figure 2.** (a) The track of Typhoon Chaba is denoted by dots from 24 September to 7 October 2016 every
128 12 hours. (b) Central pressure of Typhoon Chaba corresponding to the tracks in (a). The maximum
129 sustained wind speed is presented in red line. The green shadow band marks the time of ground-based
130 airglow observation from 20:00 LT to 04:00 LT during the night of 4-5 October 2016.



131
132

133 **Figure 3.** Consecutive satellite images of the typhoon Chaba from MTSAT-1R. The time span
134 is from 18:00 LT on 3 October 2016 to 00:00 LT on 5 October 2016, with an interval of 6
135 hours.

136 2.3 ERA-5 reanalysis data

137 ERA-5 is a fifth-generation ECMWF atmospheric reanalysis that provides hourly data
138 for many atmospheric and wave parameters. ERA-5 is produced using a four-dimensional
139 variational data assimilation algorithm based on Integrated Forecast System (IFS), with 137
140 hybrid sigma/pressure (model) levels in the vertical from 1000 hPa to 0.01 hPa (0 km to 80
141 km). More details of the model, data assimilation system, and observation data used to
142 produce ERA-5 have been described by Hersbach et al. (2020). The horizontal resolution of
143 the reanalysis temperature and wind data with a pre-interpolated resolution of $0.25^\circ \times 0.25^\circ$
144 was used in this study. Temperature perturbations were calculated by subtracting the
145 background with a 5×5 grid point running mean.



146 2.4 Ray tracing model

147 We use a ray tracing method to track the excitation source of the thermosphere
148 secondary CGWs. This model is based on the dispersion relation that considers the
149 molecular viscosity and thermal diffusivity (Vadas, 2007), as shown in Equation (1):

$$150 \quad m^2 = \frac{k_H^2 N^2}{\omega_{lr}^2 (1 + \delta_+ + \delta^2 / Pr)} \left[1 + \frac{v^2}{4\omega_{lr}^2} \left(k^2 - \frac{1}{4H^2} \right)^2 \frac{(1 - Pr^{-1})^2}{(1 + \delta_+ / 2)^2} \right]^{-1} - k_H^2 - \frac{1}{4H^2}, \quad (1)$$

151 where ω_{lr} is the intrinsic frequency; $\mathbf{k}^2 = k_H^2 + m^2$, $k_H^2 = k^2 + l^2$; k , l , and m are the zonal,
152 meridional, and vertical wave number components of the GW, respectively. The horizontal
153 wavelength (k_H) of the CGW was obtained from the ground-based airglow observations;
154 $N^2 = (g/T)(dT/dz + g/c_p)$ is the square of the Brunt-Väisälä frequency, where g is the
155 gravitational acceleration, T is the background temperature, c_p is the specific heat at constant
156 pressure, respectively; H is the scale height; $\nu = \mu/\bar{\rho}$ is the kinematic viscosity, μ is the
157 molecular viscosity, and $\bar{\rho}$ is the background density; $\delta = \nu m H \omega_{lr}$, $\delta_+ = \delta(1 + Pr^{-1})$, where Pr
158 is the Prandtl number. The background temperature T and density $\bar{\rho}$ were obtained from the
159 NRLMSISE-00 model (Picone et al., 2002).

160 The group velocity of the wave packet is formalized by Equation (2):

$$161 \quad c_{gi} = dx_i / dt = \partial \omega / \partial k_i + V_i, \quad (2)$$

162 where $V_i(u, v, w)$ is the background wind, which was obtained from the Horizontal Wind
163 Model 14 (Drob et al., 2015), and w is the vertical wind velocity, which was neglected.

164 Using Equations (1)-(2), we yield the ground-based (zonal, meridional, and vertical) group
165 velocity equation as follows (Vadas and Fritts, 2005):



$$166 \quad c_{gx} = \frac{k}{\omega_r B} \left[\frac{N^2(m^2 + 1/4H^2)}{(k^2 + 1/4H^2)^2} - \frac{\nu^2}{2} (1 - \text{Pr}^{-1})^2 \left(k^2 - \frac{1}{4H^2} \right) \frac{(1 + \delta_+ + \delta^2/\text{Pr})}{(1 + \delta_+/2)^2} \right] + u, \quad (3)$$

$$167 \quad c_{gy} = \frac{l}{\omega_r B} \left[\frac{N^2(m^2 + 1/4H^2)}{(k^2 + 1/4H^2)^2} - \frac{\nu^2}{2} (1 - \text{Pr}^{-1})^2 \left(k^2 - \frac{1}{4H^2} \right) \frac{(1 + \delta_+ + \delta^2/\text{Pr})}{(1 + \delta_+/2)^2} \right] + v, \quad (4)$$

$$168 \quad c_{gz} = \frac{1}{\omega_r B} \left\{ m \left[-\frac{k_H^2 N^2}{(k^2 + 1/4H^2)^2} - \frac{\nu^2}{2} (1 - \text{Pr}^{-1})^2 \left(k^2 - \frac{1}{4H^2} \right) \frac{(1 + \delta_+ + \delta^2/\text{Pr})}{(1 + \delta_+/2)^2} \right. \right. \\ \left. \left. + \frac{\nu^4 (1 - \text{Pr}^{-1})^4}{16H^2 \omega_r^2} \frac{(k^2 - 1/4H^2)^2}{(1 + \delta_+/2)^3} - \frac{\nu^2}{\text{Pr} H^2} \right] - \frac{\nu_+ \omega_r}{2H} \right\}, \quad (5)$$

$$169 \quad \text{where } B = \left[1 + \frac{\delta_+}{2} + \frac{\delta^2 \nu^2}{16\omega_r^2} (1 - \text{Pr}^{-1})^4 \frac{(k^2 - 1/4H^2)^2}{(1 + \delta_+/2)^3} \right], \nu_+ = \nu(1 + \text{Pr}^{-1}).$$

170 3. Results

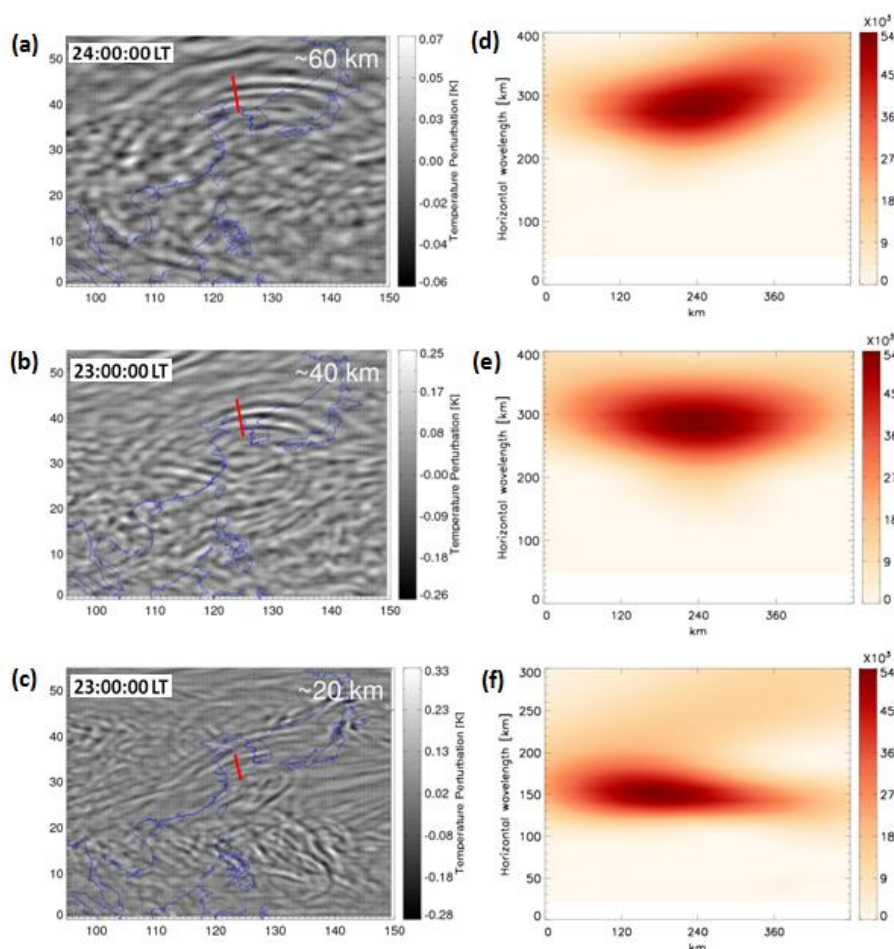
171 CGWs were observed in OH and the OI 630.0 nm airglow networks during 2-5 October
 172 and 3-4 October, respectively, during super Typhoon Chaba (2016). This study focused on the
 173 CGW event that occurred on 4 October.

174 3.1 Propagation of typhoon induced CGWs in the stratosphere

175 We extracted the CGWs excited by Typhoon in the stratosphere from the
 176 ERA-5 reanalysis data. Figure 4a, 4b, and 4c show the multilayer temperature perturbations at
 177 approximately 60 km at 24:00 LT, 40 km, and 20 km at 23:00 LT, retrieved from the ERA-5
 178 reanalysis on 4 October 2016, respectively. Figure 4d, 4e, and 4f show the corresponding
 179 wavelet analysis contours of the red line in Fig. 4a, 4b, and 4c. The temperature perturbations
 180 were calculated by subtracting the background from a 5×5 grid point running mean. The
 181 expansion area of CGW at the height of 20 km (Fig. 4c) was small, and the horizontal
 182 wavelength is approximately 150 km from Fig. 4f. Liu et al. (2014) utilized the Whole
 183 Atmosphere Community Climate model and showed that the horizontal area of the CGW
 184 expansion increases with an increase in altitude. The CGWs embraced a large area of (0° N



185 -50 °N) and (100 °E -150 °E) at approximately 60 km. The distance of the CGWs, extending
186 from the center of the circle ranged from 500 km (at approximately 20 km height) to 3000 km
187 (at approximately 60 km height). The ERA-5 reanalysis data was utilized for characterizing
188 the scale of the CGWs and indicated no small-scale fluctuation. According to the wavelet
189 analysis of Fig. 4d and 4e, the horizontal wavelength of the northward propagating CGW at
190 60 km (Fig. 4a) and 40 km (Fig. 4b) is approximately 290 km.



191
192 **Figure 4.** Temperature perturbations at (a) ~60 km at 24:00LT, (b) ~40 km, and (c) ~20 km at 23:00 LT
193 on 4 October 2016 derived from ERA-5 reanalysis. (d) the wavelet power spectrum along the red line in



194 (a), (e) the wavelet power spectrum along the red line in (b), and (f) the wavelet power spectrum along
195 the red line in (c).

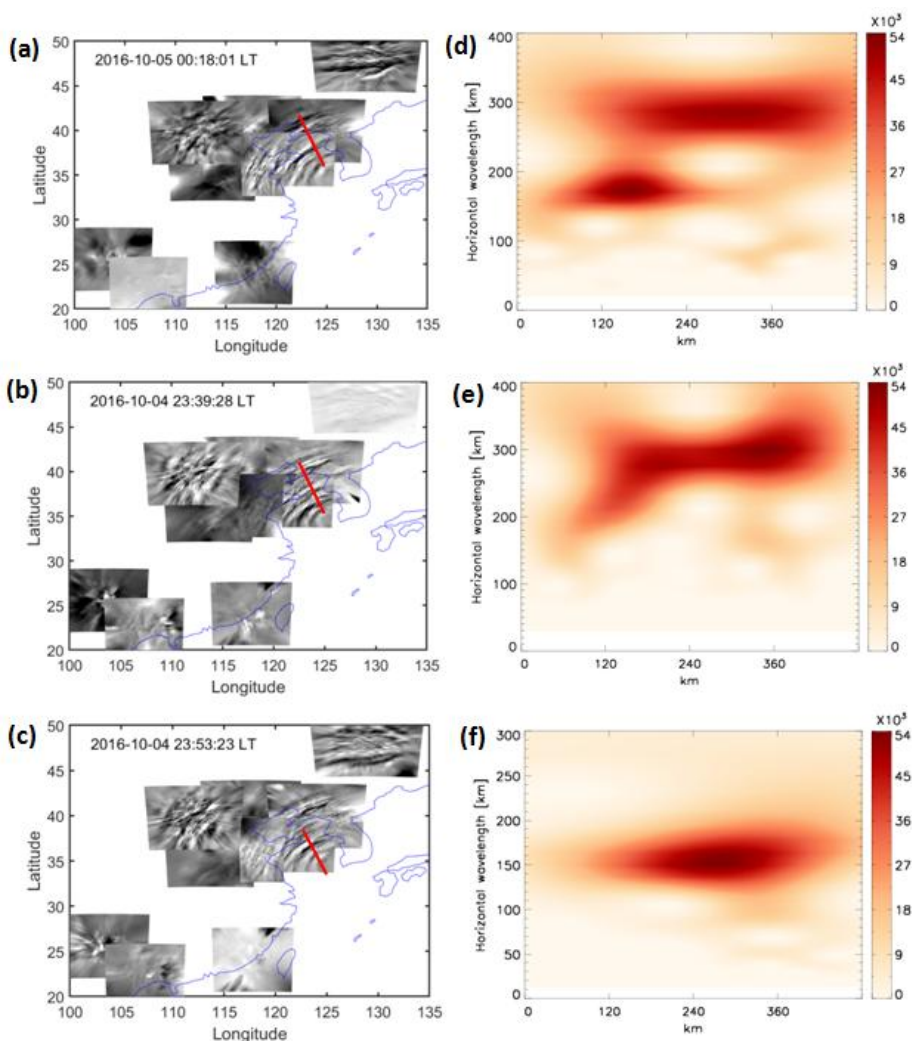
196 3.2 Propagation of typhoon induced CGWs in the mesosphere

197 As the typhoon moved along the coast of China, CGWs were identified at ten stations
198 in the OH network. Animation 1 shows that CGWs were observed by the OH airglow
199 network during 20:00–04:00 LT (the detailed data can be downloaded from the
200 Supplementary Material). As the weather conditions in North China during the study period
201 were better than those in South China, we identified clearer wave structure at the northern
202 stations compared to those at the southern stations. Nevertheless, circular wave structures
203 were visible for brief clear weather intervals at the Zhangzhou, Qujing, and Chongzuo
204 stations. The CGWs in the mesopause region extended to 2500 km, thereby nearly covering
205 the effective FOV of the OH airglow network.

206 Although the time resolution of the ERA-5 reanalysis data is only 1 h, we can use the
207 OH airglow network with a high spatial (1 km) and temporal resolution (1 min) to track the
208 CGWs at different altitudes through the reanalysis data. Compared with the single horizontal
209 wavelength of CGW at the altitude of 20 km, 40 km, and 60 km obtained by the ERA-5
210 reanalysis, the horizontal scales of CGW obtained by OH airglow network are diverse,
211 ranging from approximately 30 km to 300 km. More importantly, we found some CGWs in
212 the OH airglow layer, which are close to the CGW wavelengths at 20 km, 40 km, and 60 km
213 altitudes. In order to verify whether it is the same event, we use the group velocity to
214 estimate the time when the CGW at the altitudes of 20 km, 40 km, and 60 km reaches the
215 OH airglow layer. The times required for the CGW in the three-layer disturbance diagram in



216 Fig. 4a, 4b, and 4c reaching OH layer were approximately 18 minutes, 39 minutes, and 53
217 minutes. Therefore, the time when the CGWs at the height of 60 km, 40 km, and 20 km
218 reaches the OH airglow layer is approximately 00:18 LT, 23:39 LT, and 23:53 LT as shown
219 in Fig. 5a, 5b, and 5c, respectively. We find that the horizontal wavelength of CGW in the
220 OH airglow layer (Fig. 5c) is approximately 156 km from the wavelet analysis of Fig. 5f, the
221 observation period is approximately 23 min, and the horizontal speed is approximately 113
222 m/s, which is similar to the horizontal wavelength of the atmosphere at a height of 20 km.
223 Similarly, the horizontal wavelength of CGW in the OH airglow layer (Fig. 5a and 5b) is
224 approximately 295 km from the wavelet analysis of Fig. 5d and 5e, the observation period is
225 approximately 36 min, and the observation horizontal speed is approximately 137 m/s,
226 which is similar to the horizontal wavelength of the atmosphere at the height of 40 km and
227 60 km. This suggests that the same CGW event can be perfectly tracked at different layer
228 altitudes, and it also suggests that the CGWs in the mesosphere come from the direct
229 excitation of the typhoon.



230

231 **Figure 5.** CGWs observed by the OH airglow imager network at (a) 00:18 LT, (b) 23:39 LT, and (c) 23:53
232 LT on 4 October 2016. (d) the wavelet power spectrum along the red line in (a), (e) the wavelet power
233 spectrum along the red line in (b), and (f) the wavelet power spectrum along the red line in (c).

234

235 3.3 How does typhoon induced CGW propagate to the thermosphere?

236 Furthermore, the OI 630.0 nm airglow imager network observations at the Donggang
237 station revealed that the partial concentric ring feature lasted for 1 h from approximately

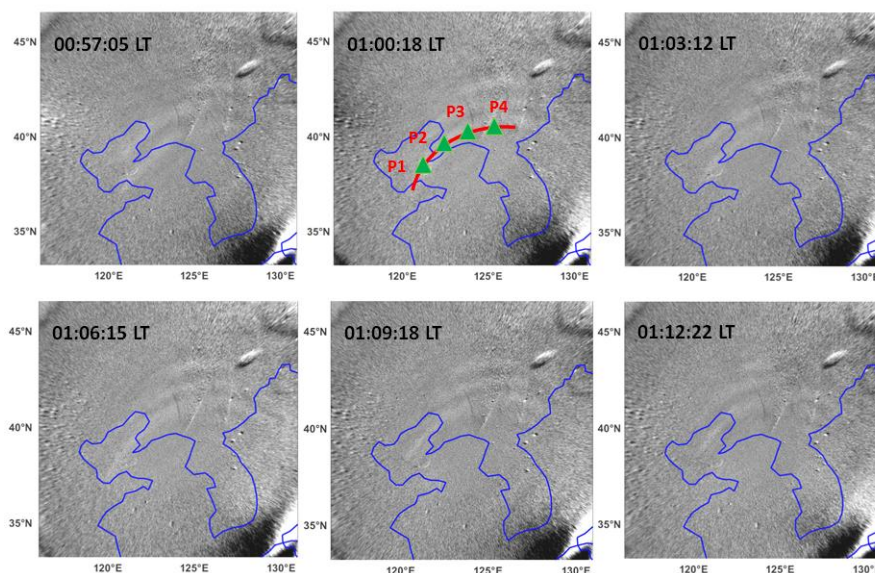


238 00:30 LT to 01:30 LT. The GWs generated in the troposphere can enter the thermosphere
239 before breaking and/or dissipating (Vadas, 2007; Azeem et al., 2015). In contrast,
240 thermospheric GWs can originate from secondary waves generated by the breaking of GWs in
241 the mesosphere (Vadas and Fritts, 2003; Vadas and Crowley, 2010; Vadas and Azeem, 2021).

242 Figure 6 shows the time sequence of the OI 630.0 nm airglow images from 00:57:05 LT
243 to 01:12:22 LT on the night of 4 October 2016. Three curved phase fronts are clearly visible.
244 The wave scale observed at the OI 630.0 nm airglow was monochromatic. It has a horizontal
245 wavelength of approximately 120 km, observed period of approximately 10 min, and
246 observed phase speed of approximately 200 m/s. The horizontal wavelength is somewhat
247 less than the multi-scale typhoon-induced concentric traveling ionosphere disturbances
248 with a horizontal wavelength from 160 to 200 km in the GNSS-TEC network as reported by
249 Chou et al. (2017). We superimposed the thermospheric CGWs on the OH airglow
250 observation images denoted by the blue arcs in Fig. 7c. The solid circles represent the
251 approximate fit of CGWs, as observed by the OH airglow network. The centre of the circles
252 is located at (31°N, 127°E), and is marked by a red dot. Compared with the single-scale
253 wave observed in the OI 630.0 nm layer, multi-scale CGWs are visible from OH network
254 observations (see Fig.7c). Nevertheless, the waves with a scale similar to that of the
255 thermosphere GWs were not identified by the OH airglow network. Moreover, compared
256 with the long-distance extension of the CGWs in the mesosphere, the propagation distance
257 of the CGWs in the thermosphere was only 600 km. Moreover, numerical simulations
258 revealed that the thermosphere GWs may originate from secondary GWs generated by the
259 breaking of primary GWs in the mesosphere or thermosphere region (Vadas and Crowley,



260 2010). We argue that the following phenomenon can represent the potential driver of this
261 pattern. Specifically, the thermospheric CGW observed by the OI 630.0 nm airglow imager
262 was not directly generated by the typhoon, but a secondary GW. To test this hypothesis, the
263 backward ray-tracing analysis was applied. In this way, we determined the source of the
264 CGW observed in the thermosphere.

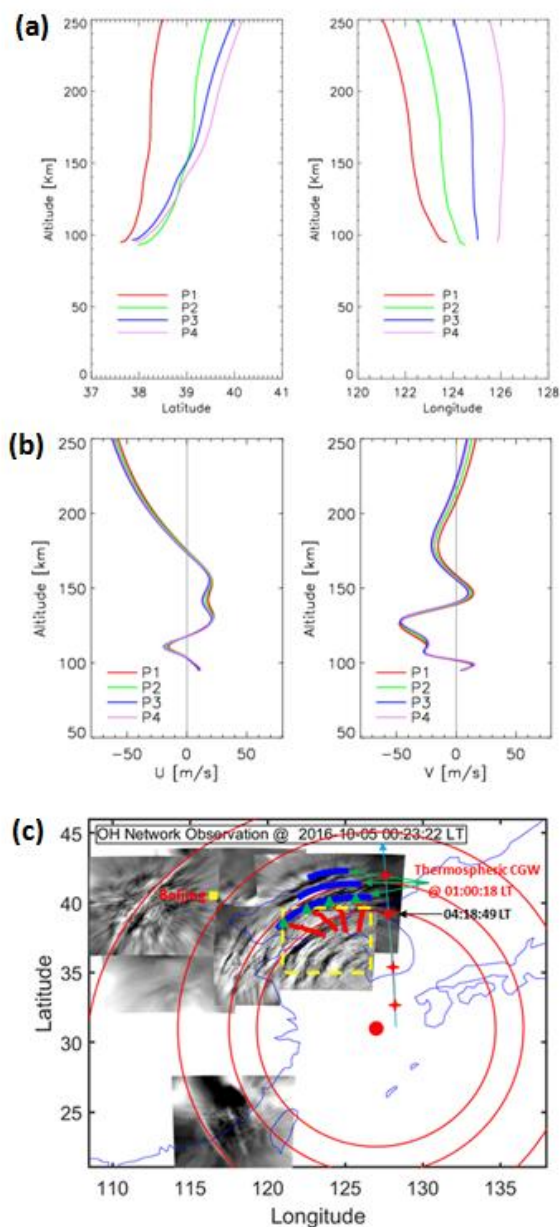


265
266 **Figure 6.** A time sequence of OI 630.0 nm airglow images observed by Donggong station during
267 00:57:05-01:12:22 LT on the night of 4 October 2016. Green triangles (P1, P2, P3, and P4) in the red arcs
268 are used as ray tracing sampling points. The blue line in each panel represents the coastline.

269 We sampled four points (green triangles) on a circular wave front (red line in Fig. 6) at
270 01:00:18 LT as the starting point for backward ray tracing. The starting height of the
271 backward ray tracing was 250 km. The ray tracing trajectories of the four sampling points
272 are shown in Fig. 7a. We used the following criterion to terminate the ray tracing that the
273 square of the vertical wavenumber should be negative. Subsequently, four backward traced
274 trajectories terminated at the altitude of approximately 95 km thereby indicating that it met



275 the reflection layer 37 min earlier. In other words, the CGW observed in the thermosphere
276 was excited at approximately 00:23 LT. The profile of the winds used in the ray tracing is
277 shown in Fig. 7b. Meanwhile, Figure 7c presents the CGWs observed by the OH airglow
278 network at 00:23:22 LT, along with the starting points (green triangles) reproduced from Fig.
279 6, and the backward ray tracing trajectories (red solid lines) from each of the starting points.
280 The ray tracing termination fell above the dissipation area of the CGW between the
281 Shandong Peninsula and the Korean Peninsula. This suggests that the CGW observed in the
282 thermosphere did not directly originate from the typhoon, but may have emerged due to the
283 dissipation of typhoon-induced CGW in the mesopause region. As the ray tracing mode used
284 in this study depends on the linear theory and does not consider the wave-wave and
285 wave-mean flow interactions and tunneling, the ray tracing results are limited and should be
286 carefully taken into consideration.



287

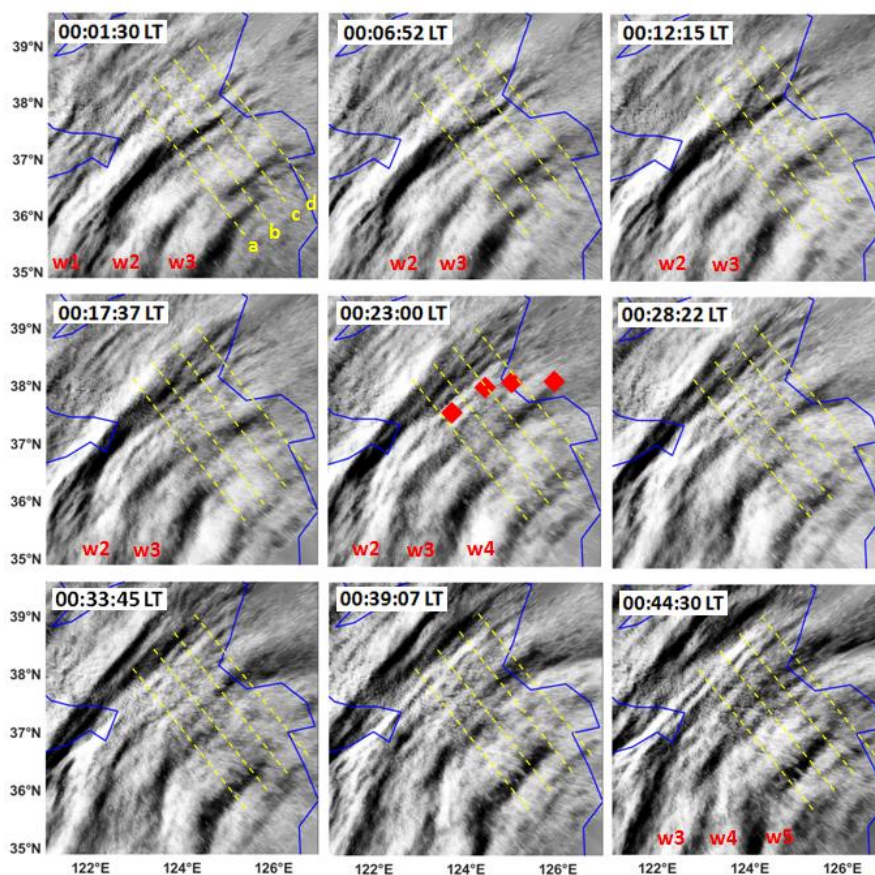
288 **Figure 7.** (a) The ray paths of the wave starting from the four sampling points in Fig.6. (b) The wind
289 profiles along the four ray-tracing paths. (c) Two layer superimposed graph: The blue arcs represent the
290 thermospheric CGW observed at 01:00:18 LT. The solid circles represent the approximate fitting CGWs
291 observed by the OH airglow network. The center of the circles is marked by a red dot. The green triangles



292 and red solid lines represent the trace start points and backward trajectories, respectively. The red crosses
293 represent the sounding footprints of the TIMED/SABER measurements. The yellow box marks the
294 location of meteor radar station.

295 **4. Discussion**

296 We showed that the strong CGWs and wave dissipating events were observed by the
297 OH airglow network both before and during the observed thermospheric CGWs on 4
298 October 2016. Figure 8 presents a time sequence of OH airglow images in the range marked
299 by the yellow dotted rectangle in Fig. 7c. The images were retrieved from the Rongcheng
300 station from 00:01:30 to 00:44:30 LT on the night of 4 October 2016. At 00:01:30 LT, three
301 distinct curved wavefronts with the wavelength of approximately 96 km were identified.
302 Interestingly, the wavefronts 2 and 3 collided and connected in the northeast, indicating
303 that nonlinear interactions may have occurred.



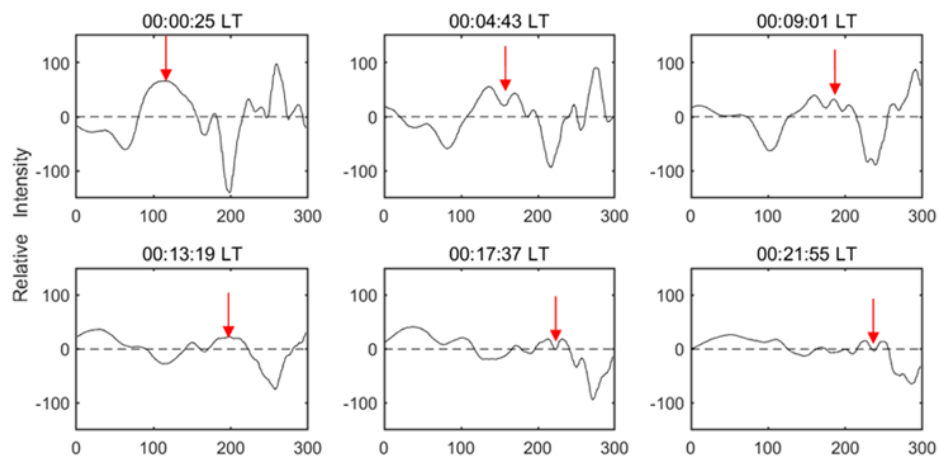
304

305 **Figure 8.** A time sequence of OH airglow images observed by Rongcheng station during
306 01:01:30-00:44:30 LT on the night of 4 October 2016. w1-w5 denote the wavefronts of the CGW. Red
307 squares denote the terminal positions of the four backward traced trajectories in Fig. 7a. The blue line in
308 each panel represents the coastline.

309 We elucidated the dissipation process of the CGW in detail by examining the evolution
310 process of its amplitude. Figure 9 shows the time series of the OH image slices
311 perpendicular to the wave fronts. As a result, we found a significant attenuation of the
312 amplitude from 00:06:52 LT to 00:21:55 LT. At 00:06:52 LT, while the relative average
313 power is 2.3×10^3 , and the amplitude decreased gradually with time. At 00:21:55 LT, the



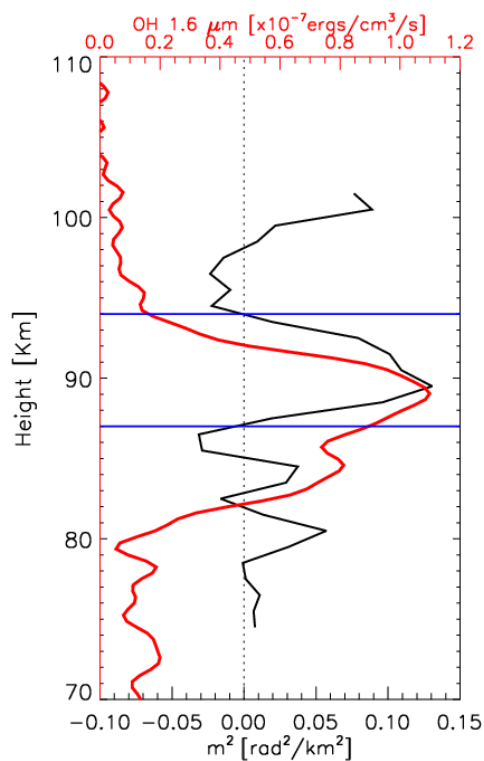
314 average power decreased to 0.14×10^3 . At the same time, we also identified the generation
315 of 20-50 km small-scale waves from the larger scales. However, the observed CGW
316 dissipation may be caused by the upward CGW passing through the airglow. Notably, the
317 observed CGW dissipation is real, unless it propagates horizontally. The propagation state
318 can be studied by using the dispersion relationship with GW, but the dissipation region of
319 the CGW lacks the real-time background temperature and wind field. In this context,
320 TIMED/SABER can be beneficial because it occurred near the wave-dissipation region;
321 however, the time lag was close to approximately 4 h. On this basis, we used the meteor
322 radar wind field data from the Beijing station as auxiliary information. We further examined
323 the dispersion relationship of GW, thereby shedding some light on the possible propagation
324 state of dissipative waves. Figure 10 presents the vertical wave number m^2 profile derived
325 from the Beijing meteor radar wind and the temperature from the TIMED/SABER sound at
326 04:18:49 LT, as marked in Fig. 7c. We identified a clear duct (from 87 km to 94 km) near the
327 peak of the OH airglow layer. Note that the duct can control the horizontal propagation of
328 CGW. This implies that the CGW may indeed be dissipated. In contrast, the upper boundary
329 of the duct coincides with the height of the ray-tracing termination area mentioned above.
330 During the wave dissipation, momentum deposition occurs in the background atmosphere
331 and can produce body forces that stimulate the secondary GWs (Fritts et al., 2006; Smith et
332 al., 2013; Heale et al., 2020).



333

334 **Figure 9.** Time series of averaged OH image slices perpendicular to the wavefronts as marked by four
335 yellow dotted lines (a, b, c, and d) in Fig. 8. The wavefronts propagate from left to right. The red arrows
336 mark the evolution of the wavefront peak.

337



338



339 **Figure 10.** Vertical wave number m^2 derived from the temperature from TIMED/SABER sound at
340 04:18:49 LT and the meteor radar wind from Beijing station marked in Figure 7c. The red line present the
341 OH 1.6 μm emission intensity obtained by the TIMED/SABER. The horizontal line represent the top and
342 bottom boundaries of the duct region.

343

344 **5. Summary**

345 In this study, a double-layer airglow network (DLAN) was used to capture the CGWs
346 over China, which were excited by the Super Typhoon Chaba (2016). We applied the ERA-5
347 reanalysis data and MTSAT-1R observations and quantitatively described the physical
348 mechanism of typhoon-generated CGWs propagating throughout the stratosphere,
349 mesosphere, and thermosphere.

350 Our analysis demonstrated that the CGWs in the mesopause region were directly by the
351 typhoon, but the CGW observed in the thermosphere may be excited by the CGW
352 dissipation in the mesosphere, rather than being directly excited by the typhoon and
353 propagated to the thermosphere. Overall, the complete propagation process of the CGWs was
354 studied and demonstrated. Specifically, it was shown how CGWs were generated by typhoon
355 in the troposphere, passed through the stratosphere, reached the mesosphere, and ultimately
356 dissipated, thereby causing the secondary wave generation, which then propagated to the
357 thermosphere.

358

359

360

361

362



363 ***Data availability***

364 The Double Layer Airglow Network data are available at <http://159.226.22.74/>. The ERA-5
365 reanalysis data are downloaded from the Copernicus Climate Change Service Climate Data
366 Store through <https://www.ecmwf.int/en/forecasts/datasets/reanalysis-datasets/era5>. The
367 typhoon information are provided at <http://agora.ex.nii.ac.jp/digital-typhoon/>. MTSAT-1R
368 data is accessed from <http://webgms.iis.u-tokyo.ac.jp/>.

369

370 ***Video supplement***

371 A video of detailed evolutions of CGWs excited by the Typhoon observed by OH airglow
372 observation network is provided (<https://doi.org/10.5446/55348>).

373

374 ***Author contributions***

375 J.X conceived the idea of the manuscript. Q.L. carried out the data analysis, interpretation
376 and manuscript preparation. H.L.L., X.L and W.Y. contributed to the data interpretation and
377 manuscript preparation. All authors discussed the results and commented on the manuscript.

378

379 ***Competing interests***

380 The authors declare no competing interests.

381

382 ***Acknowledgements***

383 This work was supported by the National Science Foundation of China (41831073 and
384 41974179), Pandeng Program of National Space Science Center, Chinese Academy of



385 Sciences and the Strategic Priority Research Program of Chinese Academy of
386 Sciences(XDA17010301), and the Informatization Plan of Chinese Academy of Sciences
387 (CAS-WX2021PY-0101).The work was also supported by the Specialized Research Fund
388 for State Key Laboratories. We acknowledge the use of data from the Chinese Meridian
389 Project.

390

391 **References**

392 Azeem, I., Yue, J., Hoffmann, L., Miller, S. D., Straka, W. C., and Crowley, G.: Multisensor
393 profiling of a concentric gravity wave event propagating from the troposphere to the
394 ionosphere, *Geophys. Res. Lett.*, 42, 7874–7880, 2015.

395 Chou, M. Y., Lin, C. C. H., Yue, J., Tsai, H. F., Sun, Y. Y., Liu, J. Y., and Chen, C. H.:
396 Concentric traveling ionosphere disturbances triggered by Super Typhoon Meranti
397 (2016), *Geophys. Res. Lett.*, 44, 1219–1226, 2017.

398 Dong, W., Fritts, D. C., Lund, T. S., Wieland, S. A., and Zhang, S.: Self - acceleration and
399 instability of gravity wave packets: 2. two - dimensional packet propagation, instability
400 dynamics, and transient flow responses, *Journal of Geophysical Research: Atmospheres*,
401 125, 2020.Drob, D. P., Emmert, J. T., Meriwether, J. W., Makela, J. J., Doornbos, E.,
402 Conde, M., et al. An update to the Horizontal Wind Model (HWM): The quiet time
403 thermosphere, *Earth and Space Science*, 2, 301–319, 2015.

404 Franke, P. M. and Robinson, W. A.: Nonlinear behavior in the propagation of atmospheric
405 gravity waves, *J. Atmos. Sci.*, 56, 3010-3027, 1999.



- 406 Fritts, D. C. and Alexander, M. J.: Gravity wave dynamics and effects in the middle
407 atmosphere, *Rev. Geophys.*, 41(1), 1003, 2003.
- 408 Fritts, D. C., Vadas, S. L., Wan, K., and Werne J. A.: Mean and variable forcing of the middle
409 atmosphere by gravity waves, *J. Atmos. Sol. Terr. Phys.*, 68, 247–265, 2006.
- 410 Fritts, D. C., B. Laughman, T. S. Lund, and Snively, J. B.: Self-acceleration and instability of
411 gravity wave packets: 1. Effects of temporal localization, *J. Geophys. Res. Atmos.*, 120,
412 8783–8803, 2015.
- 413 Fritts, D. C., Dong, W., Lund, T. S., Wieland, S., and Laughman, B.: Self - acceleration and
414 instability of gravity wave packets: 3. Three - dimensional packet propagation,
415 secondary gravity waves, momentum transport, and transient mean forcing in tidal winds,
416 *Journal of Geophysical Research: Atmospheres*, 125, 2020. Garcia, F. J., Taylor, M. J.,
417 and Kelly, M. C.: Two - dimensional spectral analysis of mesospheric airglow image
418 data, *Applied Optics*, 36(29), 7374–7385, 1997.
- 419 Gavrilov, N. M. and Kshevetskii, S. P.: Features of the Supersonic Gravity Wave Penetration
420 from the Earth's Surface to the Upper Atmosphere, *Radiophysics and Quantum*
421 *Electronics*, 61(4), 243-252, 2018. Heale, C. J., Bossert, K., Vadas, S. L., Hoffmann, L.,
422 Dornbrack, A., Stober, G., et al. Secondary gravity waves generated by breaking
423 mountain waves over Europe, *Journal of Geophysical Research: Atmospheres*, 125,
424 e2019JD031662, 2020.
- 425 Heale, C. J., Inchin, P. A., and Snively, J. B.: Primary Versus Secondary Gravity Wave
426 Responses at F-Region Heights Generated by a Convective Source, *Journal of*



- 427 Geophysical Research: SpacePhysics, <https://doi.org/10.1029/2021JA029947>,
- 428 2021.Hersbach, H., Bell, B., Berrisford, P., Hirahara, S., Horányi, A., Muñoz-Sabater, J.,
- 429 Nicolas, J., Peubey, C., Radu, R., Schepers, D., Simmons, A., Soci, C., Abdalla, S.,
- 430 Abellan, X., Balsamo, G., Bechtold, P., Biavati, G., Bidlot, J., Bonavita, M., De Chiara,
- 431 G., Dahlgren, P., Dee, D., Diamantakis, M., Dragani, R., Flemming, J., Forbes, R.,
- 432 Fuentes, M., Geer, A., Haimberger, L., Healy, S., Hogan, R. J., Hólm, E., Janisková M.,
- 433 Keeley, S., Laloyaux, P., Lopez, P., Lupu, C., Radnoti, G., de Rosnay, P., Rozum, I.,
- 434 Vamborg, F., Villaume, S., and Thépaut, J. N.: The ERA5 global reanalysis, *Q. J. R.*
- 435 *Meteorol. Soc.*, 146(730), 1999–2049, doi:10.1002/qj.3803, 2020.
- 436 Hoffmann, L., Günther, G., Li, D., Stein, O., Wu, X., Griessbach, S., Heng, Y., Konopka, P.,
- 437 Müller, R., Vogel, B. and Wright, J. S.: From ERA-Interim to ERA5: The considerable
- 438 impact of ECMWF’s next-generation reanalysis on Lagrangian transport simulations,
- 439 *Atmos. Chem. Phys.*, 19(5), 3097–3214, doi:10.5194/acp-19-3097-2019, 2019.
- 440 Holton, J. R.: The influence of gravity wave breaking on the general circulation of the middle
- 441 atmosphere, *J. Atmos. Sci.*, 40, 2497–2507, 1983.
- 442 Li, Q., Xu, J., Yue, J., Yuan, W., and Liu, X.: Statistical characteristics of gravity wave
- 443 activities observed by an OH airglow imager at Xinglong, in northern China, *Annales*
- 444 *Geophysicae*, 29(8), 1401–1410, 2011.
- 445 Liu, H.-L. and Vadas, S. L.: Large-scale ionospheric disturbances due to the dissipation of
- 446 convectively-generated gravity waves over Brazil, *J. Geophys. Res. Sp. Phys.*, 118(5),
- 447 2419–2427, doi:10.1002/jgra.50244, 2013.



- 448 Liu, H.-L., McInerney, J. M., Santos, S., Lauritzen, P. H., Taylor, M. A., and Pedatella, N.
449 M.: Gravity waves simulated by high-resolution Whole Atmosphere Community
450 Climate Model, *Geophys. Res. Lett.*, 41, 9106–9112, 2014.
- 451 Lund, T. S. and Fritts, D. C.: Numerical simulation of gravity wave breaking in the lower
452 thermosphere, 10.1029/2012jd017536, 2012. Picone, J. M., Hedin, A. E., Drob, D. P., and
453 Aikin, A. C. NRLMSISE - 00 empirical model of the atmosphere: Statistical
454 comparisons and scientific issues, *Journal of Geophysical Research*, 107(A12), 1468,
455 2002.
- 456 Sentman, D. D., Wescott, E. M., Picard, R. H., Winick, J. R., Stenbaek-Nielsen, H. C.,
457 Dewan, E. M., Moudry, D. R., Sao Sabbas, F. T., Heavner, M. J., and Morrill, J.:
458 Simultaneous observations of mesospheric gravity waves and sprites generated by a
459 midwestern thunderstorm, *J. Atmos. Sol. Terr. Phys.*, 65, 537–550, 2003.
- 460 Smith, S. M., Vadas, S. L., Baggaley, W. J., Hernandez, G., and Baumgardner, J.: Gravity
461 wave coupling between the mesosphere and thermosphere over New Zealand, *Journal of*
462 *Geophysical Research: Space Physics*, 118, 2694–2707, 2013.
- 463 Smith, S. M., Setvák, M., Beletsky, Y., Baumgardner, J., and Mendillo, M.: Mesospheric
464 gravity wave momentum flux associated with a large thunderstorm complex, *Journal of*
465 *Geophysical Research: Atmospheres*, 125, e2020JD033381, 2020.
- 466 Suzuki, S., Shiokawa, K., Otsuka, Y., Ogawa, T., Nakamura, K., and Nakamura, T.: A
467 concentric gravity wave structure in the mesospheric airglow images, *J. Geophys.*
468 *Res.*, 112, D02102, 2007.



- 469 Suzuki, S., Vadas, S. L., Shiokawa, K., Otsuka, Y., Kawamura, S., and Murayama, Y.:
470 Typhoon-induced concentric airglow structures in the mesopause region, *Geophys. Res.*
471 *Lett.*, 40, 5983–5987, 2013.
- 472 Taylor, M. J. and Hapgood, M. A.: Identification of a thunderstorm as a source of short period
473 gravity waves in the upper atmospheric nightglow emissions, *Planet. Space Sci.*, 36,
474 975–985, 1988.
- 475 Vadas, S. L., Fritts, D. C., and Alexander, M. J.: Mechanism for the generation of secondary
476 waves in wave breaking regions, *Journal of the Atmospheric Sciences*, 60, 194–214,
477 2003.
- 478 Vadas, S. L. and Fritts, D. C.: Thermospheric responses to gravity waves: Influences of
479 increasing viscosity and thermal diffusivity, *J. Geophys. Res.*, 110, D15103,
480 doi:10.1029/2004JD005574, 2005
- 481 Vadas, S. L.: Horizontal and vertical propagation and dissipation of gravity waves in the
482 thermosphere from lower atmospheric and thermospheric sources, *Journal of*
483 *Geophysical Research*, 112, A06305, 2007.
- 484 Vadas, S. L. and Crowley, G.: Sources of the traveling ionospheric disturbances observed by
485 the ionospheric TIDDBIT sounder near Wallops Island on 30 October 2007, *Journal of*
486 *Geophysical Research*, 115, A07324, 2010.
- 487 Vadas, S. L. and Liu, H.-L.: Numerical modeling of the large-scale neutral and plasma
488 responses to the body forces created by the dissipation of gravity waves from 6 h of deep
489 convection in Brazil, *J. Geophys. Res. Sp. Phys.*, 118(5), 2593–2617,



- 490 doi:10.1002/jgra.50249, 2013.
- 491 Vadas, S. L. and Azeem, I.: Concentric Secondary Gravity Waves in the Thermosphere and
492 Ionosphere over the Continental United States on 25 - 26 March 2015 from Deep
493 Convection, *Journal of Geophysical Research: SpacePhysics*, 126, e2020JA028275,
494 2021.
- 495 Walterscheid, R. L. and Hecht, J. H.: A reexamination of evanescent acoustic-gravity waves:
496 Special properties and aeronomical significance, *J. Geophys. Res.*, 108(D11), 4340,
497 doi:10.1029/2002JD002421, 2003.
- 498 Xu, J., Li, Q., Yue, J., Hoffmann, L., Straka, W. C., Wang, C., Liu, M., Yuan, W., Han, S.,
499 Miller, S. D., Sun, L., Liu, X., Liu, W., Yang, J., and Ning, B.: Concentric gravity waves
500 over northern China observed by an airglow imager network and satellites, *J. Geophys.*
501 *Res. Atmos.*, 120, 11,058–11,078, 2015.
- 502 Xu, J., Li, Q., Sun, L., Liu, X., Yuan, W., Wang, W., Yue, J., Zhang, S., Liu, W., Jiang, G., Wu,
503 K., Gao, H., and Lai, C.: The Ground - Based Airglow Imager Network in China:
504 Recent Observational Results, *Geophysical Monograph Series*, 261, 365-394, 2021.
- 505 Xu, S., Yue, J., Xue, X., Vadas, S. L., Miller, S. D., Azeem, I., et al. Dynamical coupling
506 between Hurricane Matthew and the middle to upper atmosphere via gravity waves,
507 *Journal of Geophysical Research: SpacePhysics*, 124, 3589–3608, 2019.
- 508 Yue, J., Vadas, S. L., She, C. Y., Nakamura, T., Reising, S. C., Liu, H. L., Stamus, P., Krueger,
509 D. A., Lyons, W., and Li, T.: Concentric gravity waves in the mesosphere generated by
510 deep convective plumes in the lower atmosphere near Fort Collins, Colorado, *J. Geophys.*



- 511 Res. Atmos., 114(6), 1–12, doi:10.1029/2008JD011244, 2009.
- 512 Yue, J., Miller, S. D., Hoffmann, L., and Straka, W. C.: Stratospheric and mesospheric
513 concentric gravity waves over tropical cyclone Mahasen: Joint AIRS and VIIRS satellite
514 observations, *Journal of Atmospheric and Solar - Terrestrial Physics*, 119, 83–90, 2014.
- 515 Zhou, X., Holton, J. R., and Mullendore, G. L.: Forcing of secondary waves by breaking of
516 gravity waves in the mesosphere, *J. Geophys. Res. Atmos.*, 107, 2002.